Utilizing Polymer-Grafted, Anisotropic Nanoparticles for the Design of Novel Materials

by

Thomas R. Waltmann

A dissertation submitted in partial fulfillment
of the requirements for the degree of
Doctor of Philosophy
(Physics and Scientific Computing)
in The University of Michigan
2024

Doctoral Committee:

Professor Sharon C. Glotzer, Chair
Associate Professor Qian Chen
Professor Nicholas A. Kotov
Professor Xiaoming Mao
Professor Robert M. Ziff

Thomas R. Waltmann

tomwalt@umich.edu

ORCID iD: 0000-0001-6876-5956

To mom and dad, and all those who supported me along the way

ACKNOWLEDGEMENTS

I've been so fortunate to have my graduate school experience in the Glotzer group, which is so full of talent and expertise that I was taken aback by it when I first joined. I'd like to start by thanking my advisor Sharon Glotzer, who provided me with this opportunity and helped guide me through it and onto my future endeavors every step of the way. I think in the years to come, her example of how to be a high-level professional will be as important to me as anything I've learned in graduate school. I'd also like to acknowledge the members of my committee for their help in both being collaborators and evaluating my research: Professors Qian Chen, Nicholas Kotov, Xiaoming Mao, and Robert Ziff.

Everyone else in the Glotzer group truly deserves an acknowledgment, and I'd like to start with those who I feel have had the largest impact on my own development as a scientist. Bradley Dice, for helping me navigate being a physics peep, being a mentor in both science and code development, and overall being a generous and wonderful person to be around. Thi Vo, for being a great mentor, collaborator, and always being generous with your time. Joshua Anderson, for all things related to code development; your guidance and ability to explain the complicated parts of computer science in simple ways that are easy to understand does not go unnoticed.

I'd next like to thank everyone who I've worked directly with on scientific projects. The SPOONE team of Dom Fijan, Philipp Schönhöfer, and Charlotte Zhao, we had just as much fun as we did science, which is how it really should be. I'd like

to thank my experimental collaborators from UIUC Ahyoung Kim and Xiaoying Lin for enabling the great science that we've done together. I've worked with so many other peeps while doing code development: Brandon Butler, Jens Glaser, Vyas Ramasubramani, Kelly Wang, Jen Bradley, Tim Moore, and many others. I'd also like to thank our lab manager Karen Coulter who does all the work that holds the lab together from behind the scenes.

Everyone at the University of Michigan has been so great to me, but at this point its also important to remember those who helped me get here as well. To Alex Travesset, my advisor from Iowa State, I'd like to extend the sincerest thank you for everything you did for me during my undergraduate years. To my family who have been there every step of the way, your constant support and encouragement of everything I've done academically and scientifically is more important than I can put words to.

TABLE OF CONTENTS

LIST OF FIGURES

Figure

ABSTRACT

The range of available design elements to synthesize and functionalize nanoparticle building blocks that self-assemble into superlattice structures has increased drastically over the last 30 years. From the introduction of patch interactions driven by grafting polymers to nanoparticle surfaces, to the proliferation of techniques that allow for the synthesis of a plethora of different nanoparticle shapes, we now have the experimental capability to leverage a vast toolbox of nanoscale components. For example, the shape, size, and composition of the nanoparticle core, the architecture, size, and interactions of the grafted polymers, as well as the choice of solvent, temperature, and external fields can all now be tuned experimentally. Rather than continuing to increase the variety of available nanoscale components, future work in our field will largely be focused on how to effectively utilize the nanoscale components to design building blocks that yield crystal structures with desired material properties. This work explores new ways to conceptualize and organize existing nanoscale components to advance our understanding of building block interactions for the purpose of designing novel materials.

We begin by applying polymer scaling theory to explore a new way to conceptualize polymer-grafted, anisotropic nanoparticles in the intermediate length regime. Previously, the cores of these polymer-grafted particles have been deemed entirely hard whereas the polymer shell had been considered entirely soft, creating a conceptual picture of nanoparticle assembly where the nanoparticle cores arrange themselves

according to the packing properties of their shapes and the polymer shells deform such that they are purely space filling. Utilizing the scaling theory, we explore the proposition that in the interior of the polymer shell, the polymers are rigid such that the shape of the hard core is effectively modified, altering the nanoparticle hard-core packing properties.

We next explore the use of iodine for the synthesis of polymer-grafted, gold core nanoparticles in collaboration with the Chen group at the University of Illinois at Urbana-Champaign. In their experiments, specific regions of the nanoparticle surface become occupied by iodine and are no longer accessible for polymer grafting. Using simulation models and scaling theory, we demonstrate that this synthesis technique can create building blocks with novel patch morphologies, which we then utilize for the simulated assembly of nanoparticle crystal structures.

Finally, I enumerate my scientific software contributions, which aid in finding solutions to significant problems in our field today. I begin with a set of plugins to HOOMD-blue enabling inverse design across a wider building block parameter space. Then, I discuss *agrippa*: a python package enabling end-to-end workflows for high-throughout screening of nanoparticle building block design spaces. Lastly, I discuss a new neighbor finding algorithm which may give more physically intuitive neighborhoods for systems of shaped particles.

CHAPTER I

Introduction

1.1 What is a Nanoparticle?

A nanoparticle (NP) is an object made of a few hundred atoms bonded together in some fashion whose collective size is on the nanometer length scale. NPs can be made of inorganic atoms like gold[1], cadmium[2, 3], or other metals[4, 5], or they can be organic compounds like proteins[6], viruses[7], or other biological compounds[8, 9, 10]. NPs are useful because of the unique material properties they exhibit, as well as the degree of control scientists can exert over those properties by how atoms composing the NPs are arranged. NPs are useful for their optical and electronic properties[11, 12, 13], photocatalytic properties[14, 15], thermal properties[16], and mechanical properties[17], and have a myraid of appplications, including biological applications[18, 9]. NPs are tunable via both the arrangment of the individual atoms that make up the nanoparticle (NP synthesis) and via the arrangement of NPs into colloidal crystal structures with long-range order (NP self-assembly).

1.2 Nanoparticle Synthesis

NP synthesis refers to the process of creating individual NPs by controlling the individual atoms that the NP is comprised of. Generally speaking, there are top-down synthesis techniques like milling[19], microfluidics[20], and lithography[21] which

break up larger components to produce components that are nanometers in size. There are additionally bottom-up techniques like chemical vapor deposition[22], co-precipitation[23], and others which can yield micelles[24], vesicles[25], and dendrimers[26]. Bottom-up techniques leverage the natural tendencies of the individual atoms to self-organize into nanometer length scale structures. In addition to providing a wider array of NPs with potentially new material properties, advances in NP synthesis techniques provide a wider array of design handles for use in controlling NP self-assembly behavior.

1.3 Nanoparticle Self-Assembly

NP self-assembly refers to the process by which many individual NPs assemble into bulk structures with long-range order. Methods for NP self-assembly include solvent evaporation[27, 28], interfacial and/or templated assemblies[29, 30] and the use of external fields[31, 32]. These external driving forces are often combined with molecular interactions to drive the assembly towards the desired crystal structures. NPs may be functionalized with DNA[33, 34] or other polymer chains to enhance and direct their bonding properties. For those whose goal it is to design new materials, a fundamental understanding of the physical driving forces behind the self-assembly process is essential.

In a system of particles at fixed temperature and volume, the system's free energy F is the quantity that will self-minimize and therefore governs the system's tendency to assemble. The free energy is related to both the system's potential energy and entropy by the following equation:

$$F = U - TS \tag{1.1}$$

In this equation, U is the total potential energy of the system, essentially the sum of

all the interactions among the microscopic components. In the other term, S is the entropy of the system. In systems where $U = 0$, the entropy is the number of ways to arrange the mircoscopic components without changing the macroscopic behavior. In systems of spherical NPs functionalized with polymer chains, both the polymer chain energy and entropy control much of the system's self-assembly behavior.

In more recent history, advances in chemical synthesis methods have enabled the use of nanoparticles of a wide variety of shapes[35]. Utilizing nanoparticle shape as a design handle enabled study into the self-assembly of purely hard particle systems without grafted polymers[36, 37, 38, 39, 40, 41, 42, 43, 44, 45, 46, 47, 48, 49]. In these systems, $U = 0$ and the assembly behavior is driven purely by the entropy of the particle shape. Working with purely hard particles enabled scientists in the field to combine the design handles of NP shape and grafted polymers to design new materials. This thesis focuses on how we can utilize the design handle of NP shape to control the arrangement of polymers on the surface of NPs for the design of new materials.

1.4 Outline

In Chapter II, I use simulation to investigate the predictions of a scaling theory governing the behavior of non-attractive polymers on the surface of shaped NPs across a design space of parameters including particle shape, graft density, and polymer length. This study aids in isolating the effect of NP shape on the polymer behavior as neglects attractive forces between polymers, so the polymer brush behavior on the core surface is driven largely by entropy of the polymers associated with the core shape.

In Chapter III, I work with the Chen group at the University of Illinois at Urbana-

Champaign to model their new experimental method in which anisotropic NP surfaces are doped with iodine ions that preferentially attach to different facets of the core surface, thereby altering the ability of polymers to attach to the NP surface. For this system, there are two new effects present that we must model: the effect of polymer-polymer attractions and the effect of iodine on the polymer grafting behavior. I extend my model from the previous chapter to gain a better physical understanding of what drives polymer morphology in systems where the previously mentioned driving forces in addition to NP shape are present. Once the polymer morphologies are understood, I abstract the polymer-patched NPs and simulate their self-assembly into bulk crystal structures.

Then in Chapter IV, I build on the successes of the previous chapter by modelling additional experimental knobs used to control patch morphology. In addition to particle shape, polymer-polymer attractions, polymer concentration, and iodine concentration, I now model variations in particle size and solvent quality. The first three projects in this thesis combine not only to help gain a deeper understanding of polymer behavior on shaped NPs, but also to put the effect of NP shape in context with other driving forces typically present in systems of self-assembling NPs.

In Chapter V, I discuss how computation is being leveraged in the field of NP self-assembly and present some of my code development work towards addressing outstanding problems. I present work towards solving the problem of inverse design with digital alchemy, present a package enabling high-throughput screening workflows for design in more concentrated input parameter spaces, and demonstrate a neighbor finding algorithm that may give more physically intuitive particle neighborhoods for shaped NPs.

Finally in Chapter VI, I summarize my work done in the previous chapters and

present a path forward for those who may wish to continue my work.

CHAPTER II

Creating Complex Building Block Geometry via Ligand Shell Engineering

The contents of this chapter were reproduced from a manuscript, "Creating Complex Building Block Geometry via Ligand Shell Engineering", T. Waltmann, T. Vo, and S. C. Glotzer. The manuscript is almost finalized for submission to a journal.

2.1 Introduction

Major advances in synthetic capabilities have lead to the proliferation of the use of building block shape as a driver of self-assembly [50, 51, 52, 53, 54]. This strategy leverages particle anisotropy to achieve orientationally dependent interactions between neighboring building blocks [55, 56], leading to a diverse set of self-assembled structures [57, 52, 54, 58, 59, 60, 61, 62, 63, 64]. In this same vein, computational studies have facilitated systematic exploration of the large design space of building block geometries, revealing an even richer set of structures accessible purely upon altering particle shape [65, 66, 67]. For example, numerous simulations have shown that even simple shape alterations such as vertex/edge truncation or tweaking a shape's aspect ratio can drive novel phase transformations across a diverse range of different structures [68, 67, 69]. The use of concave geometries in addition to convex ones can even drive the assembly of lock and key assemblies [70, 71, 44] with

potential applications in creating cargo-carrying or mechanically robust materials. Experimental realizations of complex particle geometries, however, remains an open challenge.

One promising approach to achieve more complex particle geometries involves manipulating not the core particle shape, but rather the ligand shell coating the particle. Ligand coatings are commonly employed in stabilizing particle dispersion in solutions [52, 72, 73, 74] and are of interest in light of recent experimental works showing that the shape of the ligand shell can differ from that of the core [61, 75, 76]. Thus, engineering the shape of the ligand shell provides a promising route to program systematic shape alterations to core particle geometry such that the shape of the composite particle (core + ligand shell) is one that exhibits previously inaccessible building block geometries.

In this work, we use scaling theory [61, 75] to *a priori* predict the shape of a ligand shell coating an anisotropic NP core as a tool for designing building blocks exhibiting novel *effective shapes*. The scaling theory predicts three regions of ligand conformation as a function of distance from the core surface – concentrated, semi-dilute, and dilute [61]. The ligands are flexible in both the semi-dilute and dilute regimes with monomer densities $\rho < 1$, but in the concentrated regime the monomer density approaches one. This dense layer nearest the surface of the particle acts as a non-deformable shell about the core and we define the outermost boundary of this region (particle core + concentrated ligand regime) as the *effective shape*.

The scaling theory treats ligands as linear polymeric grafts of length N and grafting density σ anchored at one end to the surface of a convex particle [61]. Following the theoretical development in Refs. [61, 75], we predict the *effective shape* of the ligand-grafted particle by introducing an anisotropy parameter Ω defined over all

points on the surface of the particle core as $\Omega(\theta, \phi) = |\vec{r}(\theta, \phi)|/r_{in}$, where r_{in} is the insphere radius of the core. Ω thus serves as a metric for the local curvature of the core particle. Locations of higher curvature afford more freedom to flexible ligands due to increased chain entropy [77, 78], and free energy minimization will produce an equilibrium ligand distribution that is generally non-uniform, producing an *effective shape* that is not necessarily conformal to the underlying core particle shape. Through judicious choice of ligand length and grafting density, the *effective shape* can be tuned to a desired shape to produce new building block geometries. Here, we predict the range of *effective shapes* accessible across relevant experimental parameters such as ligand length and grafting density for four commonly synthesized core geometries – cube, octahedron, rhombic dodecahedron and pentagonal bipyramid. We validate the scaling theory predictions by direct comparison with molecular simulations. We then show that such *effective shapes* can drive interesting self-assembly behavior by showcasing the assembly of a lock and key structure that would have been inaccessible using the bare core geometry. Our results highlight how design of the ligand coating around the core particle can serve as a handle for the design and synthesis of more complex particle geometries as well as new self-assembled colloidal superlattice structures.

2.2 Methods

Below we describe the methods underlying our theoretical calculations, molecular dynamics simulations, and Monte Carlo simulations. All simulations were performed using the HOOMD-Blue [79] simulation package. We used the *freud* [80] simulation analysis library and managed our data with the *signac* [81] data management framework.

2.2.1 Ligand-Coated Nanoparticle Simulations

To validate our theoretical predictions, we performed coarse-grained molecular dynamics simulations of ligand-grafted nanoparticles whose anisotropic core can take one of the four polyhedral shapes previously mentioned. Each core shape has an insphere diameter of approximately $\sigma_s = 2R_0 \approx 10$, corresponding to a shape with surface area of 600, with f grafted ligands ranging from $f = 50$ to $f = 400$ and degree of polymerization N ranging from $N = 5$ to $N = 50$. One end bead of each ligand is constrained to move on the surface of the core using the Anisotropic Lennard Jones (ALJ) potential [83]. Briefly, the ALJ potential takes the form:

$$U_{ALJ} = 4\epsilon_s \left[\left(\frac{\sigma_s}{r}\right)^{12} - \left(\frac{\sigma_s}{r}\right)^{6} \right] + 4\epsilon \left[\left(\frac{\sigma_c}{r_c}\right)^{12} - \left(\frac{\sigma_c}{r_c}\right)^{6} \right] \tag{2.1}$$

ALJ simulates interactions between anisotropic particles by applying both a potential between particle centers and a contact potential between the closest surface points on two interacting particles. The parameter σ_c defines the range of the contact potential, which we set to be equal to $0.15\sigma_s$. The parameters r and r_c are the distances between particle centers and between the closest two points on interacting particles, respectively. The parameter ϵ_s is defined by the potential to be proportional to ϵ in a way that preserves the core shape as the distance between particles increases.

Pair interaction strengths were set to $\epsilon = 1$ in units of k_BT for all pairs except for core-graft interactions, which use $\epsilon = 100$ to keep the ligands constrained to the surface of the core. We use interaction cutoffs equal to $2^{1/6}\Omega\sigma_s$ and $2.5\Omega\sigma_s$ for WCA interactions and interactions with an attractive well, respectively. Bonded monomers ($\sigma_s = 1.0$) are connected using the standard FENE bond of the form [84]:

$$U_{FENE} = -\frac{1}{2} k r_o^2 \ln \left[1 - \left(\frac{r}{r_o}\right)^2 \right] \tag{2.2}$$

where $k = 70$ and $r_o = 1.725$. These FENE bond parameters were selected to en-

sure that the ligand's radius of gyration (R_g) follows the scaling behavior expected of a polymer in a good solvent: $R_g \sim bN^{3/5}$ (see SI) [85] and to ensure ligand monomers cannot unphysically cross one another. Results for the cube, octahedron, and rhombic dodecahedron are discussed in the main text. Due to its high aspect ratio, the pentagonal bipyramid required an extension of the developed scaling theory; this extension and the corresponding results are highlighted in the SI. For all core shapes, the surface area was kept at a constant value of 600. Our simulations were all performed in the NVT ensemble for 1×10^7 timesteps with $kT = 1.0$ and $\partial t = 0.0005$.

2.2.2 Scaling Theory Methods

We implemented the scaling theory from refs [61, 75] into a new python package named *agrippa*[82] for calculating effective shapes and their lattice energies. The *agrippa* package provides an easy-to-use interface for effective shape calculations and is discussed at length in Chapter V. All effective shapes in this work were calculated via the *agrippa* package using the same number of grafts f, particle sizes σ_s, and number of monomers N for running simulations in the previous paragraph. We use monomer bead sizes equal to 0.89 rather than 1.0 for the scaling theory calculations because the minimum of the FENE bond potential with parameters from the above paragraph is 0.89.

2.2.3 Effective Shape Self-Assembly Simulations

As one case study, we ran hard particle Monte Carlo (HPMC) simulations of a binary system of one selected effective shape - a "scooped cube" - and a larger number of much smaller spheres. We assume all interactions in the system are excluded volume interactions, typical of a theta solvent condition in experiment.

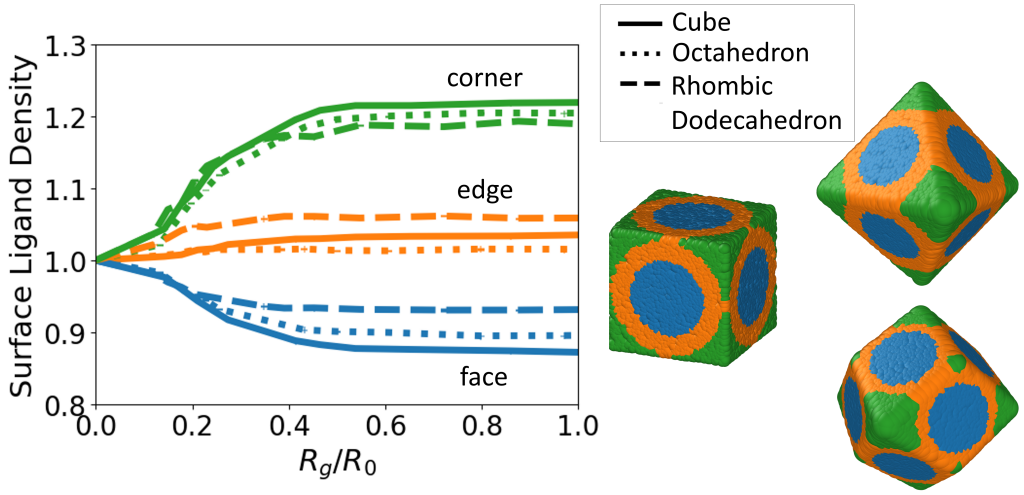

Figure 2.1: Simulated ligand grafting densities relative to $\rho(N = 0)$ (uniform coating) for different core regions with $f = 100$ ligands, demonstrating how partitioning of the ligands to the three regions changes with increasing ligand length. Normalizing the density by the maximum value of the curvature parameter Ω for each shape allows us to compare the data across all three particle shapes (Table. 2.1). Increasing ligand length produces increased affinity for the corner regions (green), reduced affinity for the face regions (blue), and a small increased affinity for the edge regions (orange). The unequal partitioning of ligands within the three regions reaches its maximum when the radius of gyration is roughly half the radius of the core insphere. The three particle images provide a visual depiction of how each region is defined on each of the three core shapes, and we define each region mathematically in Table 2.1. We attribute differences in the curves for the same region on different shapes to slight differences in how these regions are defined. Error bars are less than the width of the lines.

The size and stoichiometry of the spheres and scooped cubes are such that the volume ratio $V_{sphere}/V_{cube} = 0.0027$ and the stoichiometry is $6 : 1$. HPMC simulations were performed in the NVT ensemble with 7000 total particles (1000 scooped cubes, 6000 spheres). The system was initialized at a particle volume fraction of $\phi = 0.05$ and progressively compressed to $\phi = 0.7$. At each target volume fraction, we performed a production run of 1×10^7 MC sweeps, with four trial moves attempted per particle per sweep.

2.3 Results

2.3.1 Ligand Surface Distribution

The effective shape of the ligand shell coating a nanoparticle depends upon several factors, the first of which is the spatial distribution of the ligands on the surface of the particle. For non-spherical particles, the ligands are not distributed uniformly[77]. To calculate the surface probability distribution of the ligands as a function of ligand length N and fixed nanoparticle size and shape, we first partitioned the surface of each shape into regions by the local curvature parameter $\Omega(\theta, \phi) = |\vec{r}(\theta, \phi)|/r_{in}$. Each shape was divided into three regions: face, edge, and corner. A table defining the ranges of Ω for each region is given in Table 2.1 and visualizations of the three different regions for each shape are shown in Fig. 2.1. We computed the density of ligands at their grafting point, ρ, from simulation in each region and plotted the ratio of the surface density relative to the $\rho(N = 0)$ limit where the surface distribution is uniform (Fig. 2.1).

Scaling theory predicts that increases in ligand length will induce ligands to preferentially attach on the high curvature regions of the core surface[86]. Our simulations (Fig. 2.1) demonstrate that the entropy gain from partitioning to high curvature regions of the core surface becomes significant once the ligands reach a threshold length ($R_g/R_0 \approx 0.1$), at which point the relative affinity for the different regions on the particle core increases until it reaches a maximum value ($R_g/R_0 \approx 0.5$). The initial change in affinity ($R_g/R_0 \approx 0.1$) demonstrates qualitative agreement with scaling theory because of the preferential attachment to higher curvature regions. The asymptotic nature of the affinity change ($R_g/R_0 \approx 0.5$) reflects saturation of surface sites available in the preferred, high curvature region. Changes in density shown in the figure are normalized by the maximum value of Ω for each shape, al-

lowing us to compare across different shapes and demonstrating the universality of the ligand partitioning behavior across all three shapes. We attribute the slight differences between shapes to the slight differences in how the corner, edge, and face regions are defined on the different shapes (see Fig. 2.1, right).

2.3.2 Density Profiles Away From NP Surface

In addition to the spatial distribution of ligands on the surface of the particles, the effective shape depends on the density of the ligand monomers as the chains extend outward from the core surface. As shown in Fig. 2.2, we compute the monomer density profile, ρ, in the simulated systems as a function of radial distance from the center of the particle, where the x-axis is scaled by $\Omega^{3/2}$ to account for the local curvature. Our results demonstrate that increasing N leads to the emergence of a secondary regime (around $N = 40$) towards the tail end of the density profile, reflective of a transition from a stretched ligand conformation nearer to the surface to a more relaxed conformation of the outermost monomers on the ligand chain. The height of the density peak varies with shape, but does not vary with N (Fig. 2.2d,e,f), indicating that a densely packed regime is always present closer to the core particle surface. We attribute differences in peak heights between the different shapes to different curvatures of the core geometries. As shown in Fig. 2.2g,h,i, increasing the ligand graft density σ results in a corresponding increase in the height of the density profile peak. This increase is due to higher ligand chain stretching near the surface to accommodate additional ligands, producing a more concentrated regime that augments the local monomer density. As we move further away from the core surface, the ligands have more accessible local volume and revert back to exhibiting the behavior expected of a relaxed ligand chain. The above trends demonstrate the existence of multiple polymer scaling regimes within the polymer brush marked by

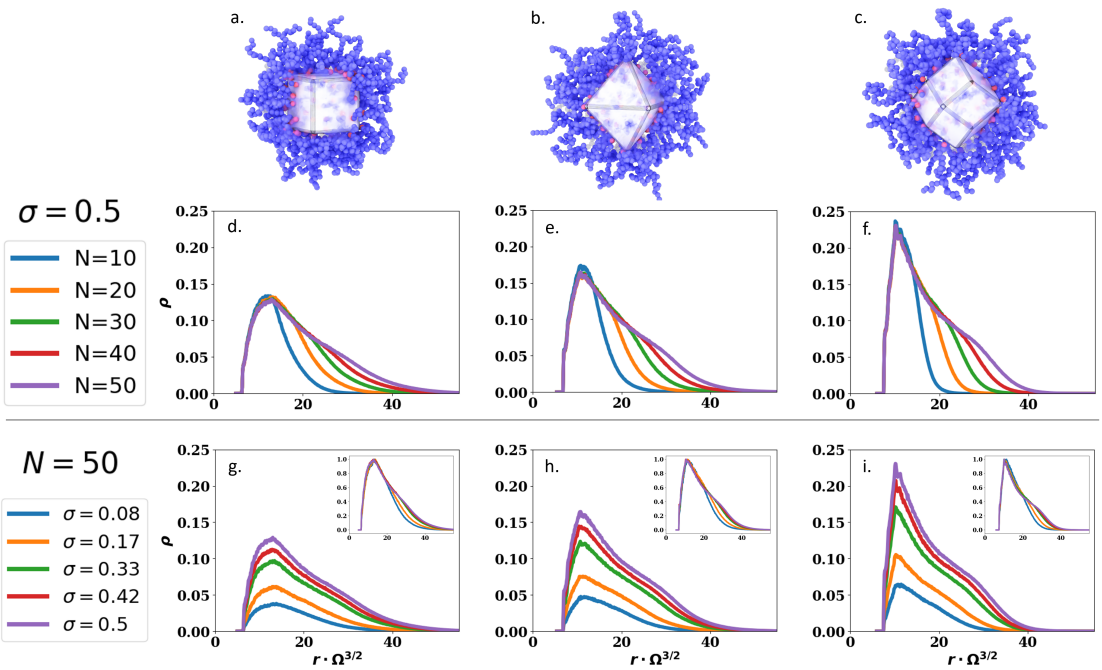

Figure 2.2: Simulation snapshots (a-c) and monomer density profiles (d-i) across a range of ligand densities and ligand lengths for the cube, octahedron, and rhombic dodecahedron, respectively. As the number of monomers N on a ligand chain increases at constant graft density σ (d,e,f), the profile extends further outward and changes slope. As σ increases at constant N (g,h,i), the peak density and distance the ligand brush extends from the core increases. The insets in parts g,h, and i normalize the peak heights, demonstrating the change in slope seen in parts d,e, and f also happens as σ increases.

a visible transition in the density profile between the concentrated regime and the unswollen/swollen regimes, consistent with assumptions of scaling theory regarding polymer chain scaling behavior.

2.3.3 Effective Shapes

We next computed the effective shapes of the simulated ligand coated nanoparticles to compare with scaling theory. Briefly, effective shapes are computed from simulation by determining the monomer on each ligand chain that first deviates significantly from a straight extension away from the centroid of the core particle. The positions of those monomers create a point cloud that defines the surface of the effective shape, see Fig. 2.7 for more information.

As shown in the left-hand column of Fig. 2.3, we observed four effective shape classes across both simulation and scaling theory, which we refer to as rounded, conformal, spiky and scooped. "Rounded" effective shapes are characterized by rounded convex faces. "Conformal" effective shapes are conformal to the core's geometry. "Spiky" effective shapes are characterized by significant partitioning of the ligands preferentially to the corners, giving the appearance of spikes located at the core's vertices. "Scooped" effective shapes have significant partitioning of the ligands preferentially to both edges and corners, creating concave surfaces on the particle facets. In short, the rounded effective shape is a convex perturbation of the core shape, the spiky and scooped effective shapes are concave perturbations of the core shape, and the conformal effective shape reflects the underlying core shape.

Comparison of the effective shape classes between simulation and theory across different anisotropic core particle shapes and physically relevant parameter values are shown in the right-hand column of Fig. 2.3. We see that the location in shape diagram of each effective shape class appears largely independent of core geometry. In general, we find two common features. First, as ligand length is increased, the effective shape undergoes a smooth transition from the convex to concave effective shapes as a result of the expected entropically driven preferential ligand partitioning to high curvature regions of the core shape. Short ligands, conversely, distribute more uniformly on the core surface. In the limit of short ligands, a uniform graft distribution combined with increased stretching of the ligand chain close to the particle facets due to increased crowding (relative to vertices and edges) produce the observed convex effective shape. At long ligand length, the ligands aggregate near the vertices of the shape to gain entropy, thereby creating a non-uniform distribution, giving rise to a concave effective shape. It is important to note that the transition from a convex to a concave effective

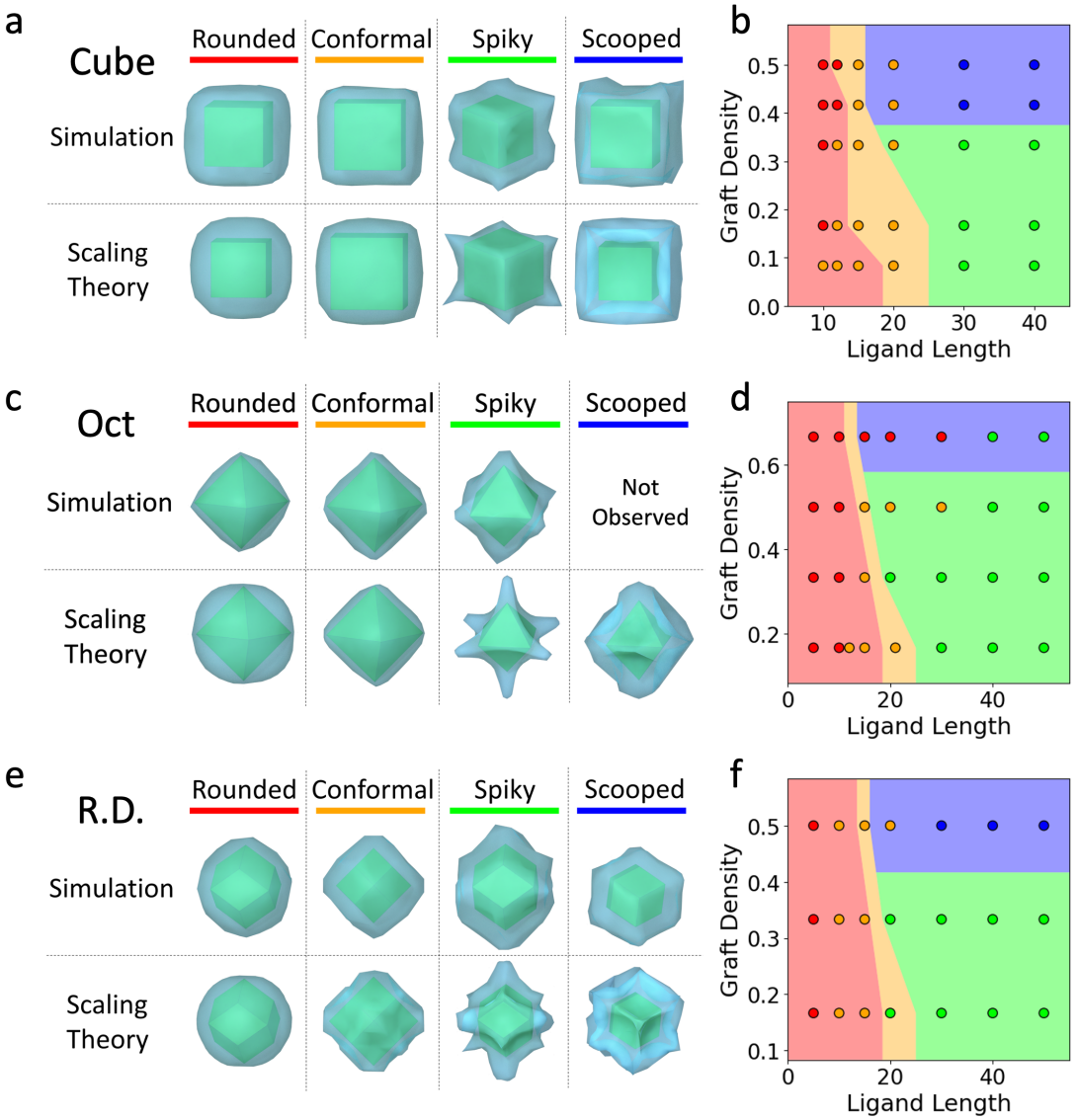

Figure 2.3: Effective shape diagrams (b,d,f) for the cube (a,b) octahedron (c,d) and rhombic dodecahedron (e,f). Each diagram contains four effective shapes: rounded (red), conformal (orange), spiky (green), and scooped (blue). The background colors indicate the effective shape predicted by theory, and the colored circles indicate the effective shape observed in simulation. Effective shape classes (a,c,e) as computed in simulation and predicted by theory for the corresponding shapes. Effective shapes are indicated by the outer surface of the blue regions around the green nanoparticle cores. The blue regions correspond to the densest regime in the ligand distribution.

shape is a smooth one, and we can therefore understand the conformal effective shape as the intermediate between convex and concave.

The second common feature we observed in the MD simulations is that increasing ligand grafting density for long ligands creates a smooth transition from spiky to scooped concave effective shapes. In the spiky shape, the ligands have already preferentially partitioned and saturated surface locations associated with the corners. As such, the next most entropically favorable locations are the edges of the core particle. Gradual edge partitioning merges together individual corner spikes as the effective shape changes from spiky to scooped (see Fig. 2.8). It is important to note that we did not observe the formation of the scooped phase in either the octahedron (Fig. 2.3, middle) or the bipyramid (Fig.2.10) system in simulations. We conjecture that these shapes may exhibit the scooped phase at a higher graft density; however, we cannot simulate higher graft densities while maintaining ergodicity of the ligands to explore the entire surface of the core shape.

2.3.4 Entropic Assembly of Effective Shapes

In this section, we demonstrate the successful self-assembly of a binary system consisting of scooped cubes and smaller spheres into a lock and key structure that would otherwise be inaccessible with the unperturbed core shape. We use this one example case to demonstrate just one of the many lock-and-key type crystals possible from these effective shapes.

We neglect all interactions other than excluded volume so that entropy maximization is the driving force for assembly. On their own, scooped hard cubes assemble into orientationally misaligned planes of a simple cubic crystal (Section 2.5.6) with open gaps at each concave face-face contact. We hypothesize that sufficiently small spheres might fill the gaps and remove the orientational misalignment between planes, form-

ing a colloidal crystal structure whose primitive unit cell has an ideal stoichiometric ratio of three spheres to one scooped cube. We performed HPMC simulations at an off-stoichiometric ratio of 6:1 as previous work has shown that an excess of small particles can enhance nucleation and growth of the stoichiometrically preferred (here, 3:1) crystal structure in binary, purely entropic systems [87].

In the scooped cube / sphere system, the scooped cubes ordered into the expected simple cubic lattice at $\phi \sim 0.5$ (Fig. 2.4, lower right), similar to previously reported assembly behaviors of hard cubes [88, 65, 66]. However, there are significant gaps between the cubes that allow for high sphere mobility throughout the structure; the gap size decreases with increasing particle volume fraction (Fig. 2.4, top). We quantified the effect of gap size on sphere localization and mobility, defining spheres to be localized during the time they are in the concave region of at least one of the cubes. Increasing particle volume fraction results in a larger fraction of the spheres being localized (Fig. 2.4, lower left, red curve). At the highest particle volume fraction, $\sim 75\%$ of spheres are localized whereas in the ideal structure, where one sphere sits in each gap, only $\sim 50\%$ of spheres would be localized. This means that the system has self-assembled into the targeted binary colloidal crystal structure, albeit with a ratio of 4.5 spheres to 1 cube instead of the ideal 3:1 ratio. By inspection of the simulations, we note that the numbers of spheres in a single gap can vary between $0 - 6$.

Although localization is an indicator that spheres are trapped in the concave regions of the cubes, there is also the possibility that the spheres are hopping from gap to gap, and thus are momentarily localized but not immobile. To further delineate between mobile and immobile localized spheres, we first record for a given snapshot the reference cubes to which each sphere is localized. We then track in subsequent

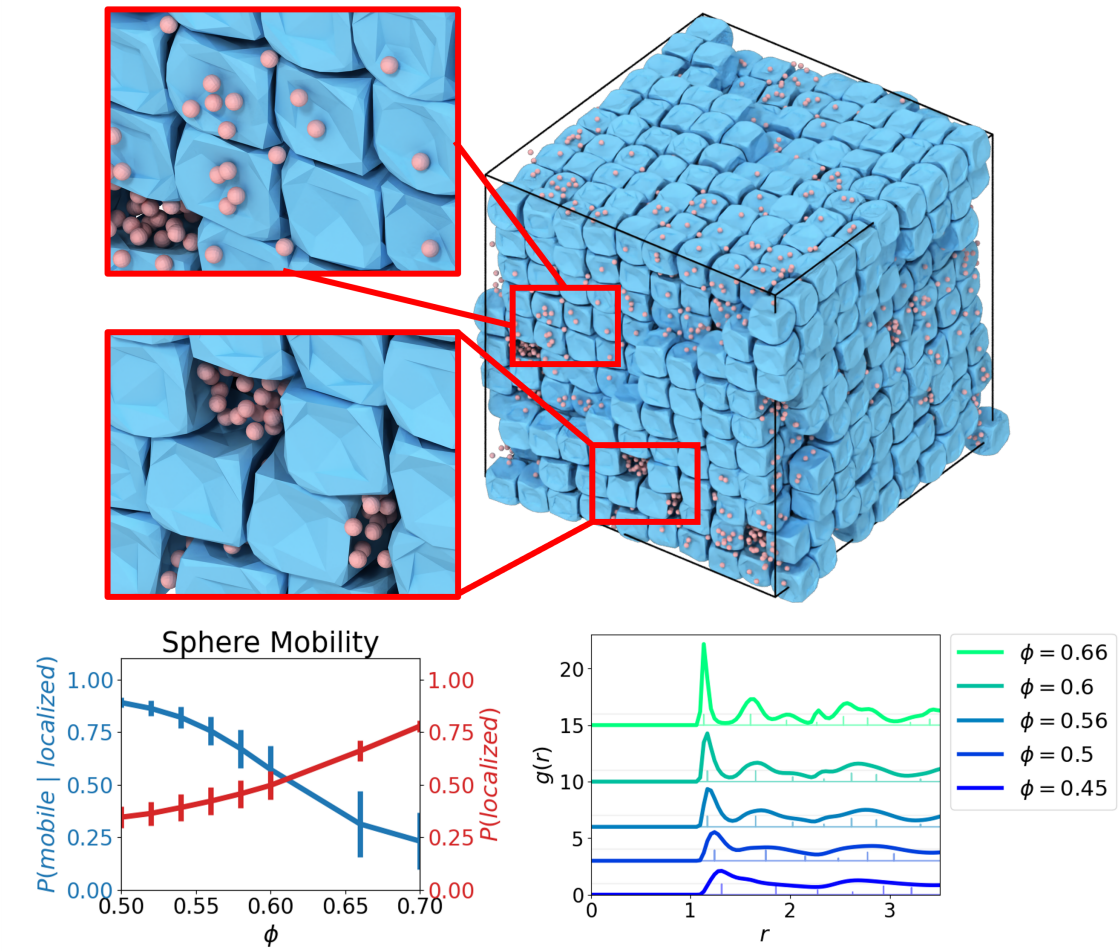

Figure 2.4: System of scooped cubes and small spheres at a volume fraction of $\phi = 0.66$ (top). The insets highlight spheres that are localized in the concave face-face contacts between spheres across periodic boundary conditions (upper) and other spheres that aggregate in open lattice sites (lower). The radial distribution function (RDF) is calculated for the scooped cubes only and demonstrates their assembly into a noisy simple cubic structure at volume fractions ranging from $\phi = 0.5$ to $\phi = 0.66$ (bottom right). Mobility of spheres is indicated in the lower left plot. The red axis indicates the fraction of spheres that are localized inside the concave regions of the scooped cubes. The blue axis indicates the fraction of localized spheres that are still able to move throughout the system. The two quantities are inversely proportional, indicating that at the highest filling fraction the spheres are largely trapped (localized indefinitely) inside the concave regions of the scooped cubes.

snapshots the fraction of spheres that move into or out of gaps associated with each reference cube. This allows us to measure the fraction of spheres that remain mobile even though they are momentarily localized after entering a gap (Fig. 2.4, lower left, blue curve). From the lower left plot in Fig. 2.4, it is clear that increases in particle volume fraction not only increase localization, but also decrease sphere mobility. At the highest particle volume fraction, we see that $\sim$ 25% of the localized spheres can still move from one cube to another. This value of 25% corresponds to spheres that are localized around a single cube, but have no matching cube to seal off the concave region, preventing encapsulation. We speculate that this mobile cohort of spheres further increases the entropy of the system. Thus we have shown that we can leverage the additional space afforded by effective shape concavity to drive the co-assembly of a lock and key structure that would have been inaccessible using the native core geometry.

2.4 Conclusions

In this work, we investigated the behavior of non-attractive ligands grafted to anisotropic cores through scaling theory and molecular simulation. We first determined the conditions underlying the expected, entropy-driven ligand partitioning to regions of high curvature on the core particle's surface. Through analysis of monomer density profiles, we confirmed the existence of a dense region of monomers where the sections of the ligand chains closest to the particle surface are immobile, effectively forming an extension of the core to produce an *effective shape*. We then characterized the *effective shape* for a wide range of experimental design parameters such as ligand length, core geometry, and ligand grafting density to determine four classes of effective shapes: rounded, conformal, spiky, and scooped. Lastly, we leveraged the

concave effective shape to drive the co-assembly of a binary lock and key structure in which smaller spherical particles are localized in the gaps between scooped cubes. Our results show that the ligand shell of a nanoparticle can be engineered to adopt one of several classes of effective shapes that can subsequently be exploited to drive the assembly of interesting binary co-crystals. Importantly,these complex building block shapes can be accessed by tuning experimentally accessible design parameters.

2.5 Supplementary Information

2.5.1 Determine Simulation Model Parameters

Simulation model parameters for this study were not obtainable from previous literature because our simulations used the relatively new Anisotropic Lennard-Jones potential[83]. There are no other studies that use this potential to model ligand chains, so we completed a parameter sweep to determine which parameters give the correct scaling behavior. We expect to see a ligand chain scaling exponent $\nu = 0.6$ in the part of the ligand the implicit solvent can penetrate. To this end, we completed a parameter sweep across different bond types and bond parameters, including harmonic and FENE bond potentials. For each parameter statepoint we ran a simulation at different values of the ligand length $N = 50, 75, 100, 125$, computed R_g, and fit the equation

$$R_g \sim bN^{\nu} \implies \log R_g \sim \nu \log N \tag{2.3}$$

to the part of the ligand after the second slope change in the density profile. This is the section of the ligand the implicit solvent should penetrate, and where we expect to see swollen ligand chain behavior.

To determine the ligand scaling exponent ν, we use a log-log plot where the slope of a linear fit is ν. The parameter choice of the FENE bond potential with

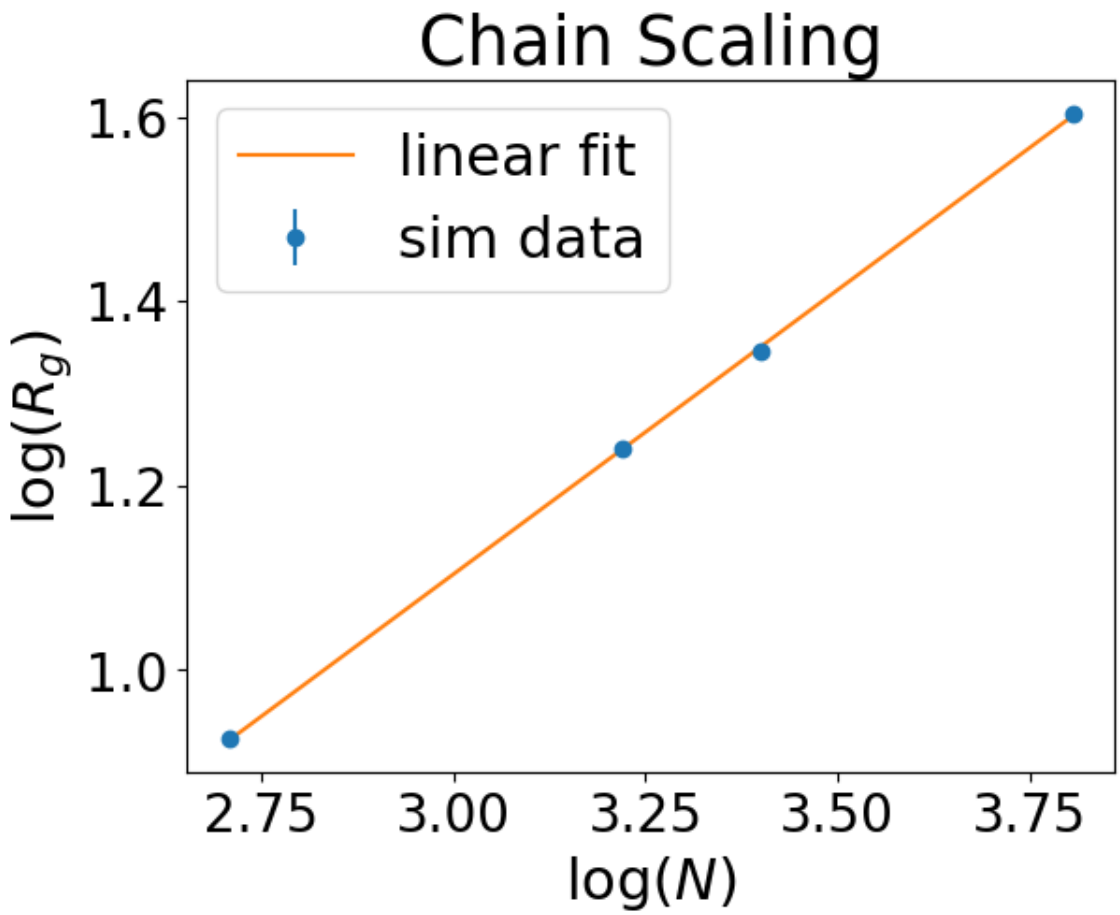

Figure 2.5: Log-log plot used to determine the scaling exponent our ligands. In blue is the scaling data computed from simulation. In orange is the linear fit, which has a slope $\nu = 0.616$. Errors bars are less than the width of the blue dots.

$k = 70$, $\epsilon = 0.5$, and $r_0 = 1.5\sigma_{\text{FENE}}$ produces the plot in Fig. 2.5, which has a slope $\nu = 0.616 \pm 0.005$.

2.5.2 Surface Ligand Distribution

We divide the surface of our shape into regions we call face, edge, and corner based on cutoff values in the curvature parameter Ω. We enumerate the range of Ω for which we define each region of the shape in Table 2.1.

In the main paper, we detailed how changes in ligand *length* result in changes in the surface ligand distribution. In this section, we detail how changes in ligand *density*

Table 2.1: Curvature parameter Ω boundary values.

Shape	**Face**	**Edge**	**Corner**
Octahedron	1.0, 1.15	1.15, 1.35	1.35, 1.732
Cube	1.0, 1.2	1.2, 1.414	1.414, 1.732
Rhombic Dodecahedron	1.0, 1.12	1.12, 1.2	1.2, 1.414

translate to changes in the surface ligand distribution. In Fig. 2.6 we show how the affinity for the corners changes as σ changes. The plot demonstrates that lower ligand density nanoparticles change their affinity for the corners by more than the larger ligand density nanoparticles, and need longer ligands to reach the maximum corner affinity. The data supports the idea that ligands pack the corner areas of the nanoparticle surface to some maximum density after which the density cannot increase further. Higher ligand density nanoparticles reach this maximum density at their corners quicker, and the relative change in density is smaller because larger ligand density nanoparticles start closer to maximum packing on the corners.

2.5.3 Computing the Effective Shapes from Simulations

We computed the effective shape of our nanoparticles from simulation data in the following way:

Algorithm:

- create 3d histogram h for binning points in space
- for each frame in the simulation after equilibration:
  - for each ligand index i on the nanoparticle:
    - get a unit vector $\vec{u}_{g_i}$ in the direction of the graft monomer g_i on ligand i
    - find the first monomer m_j on the ith ligand such that $\vec{u}_{m_j} \cdot \vec{u}_{g_i} < .97$

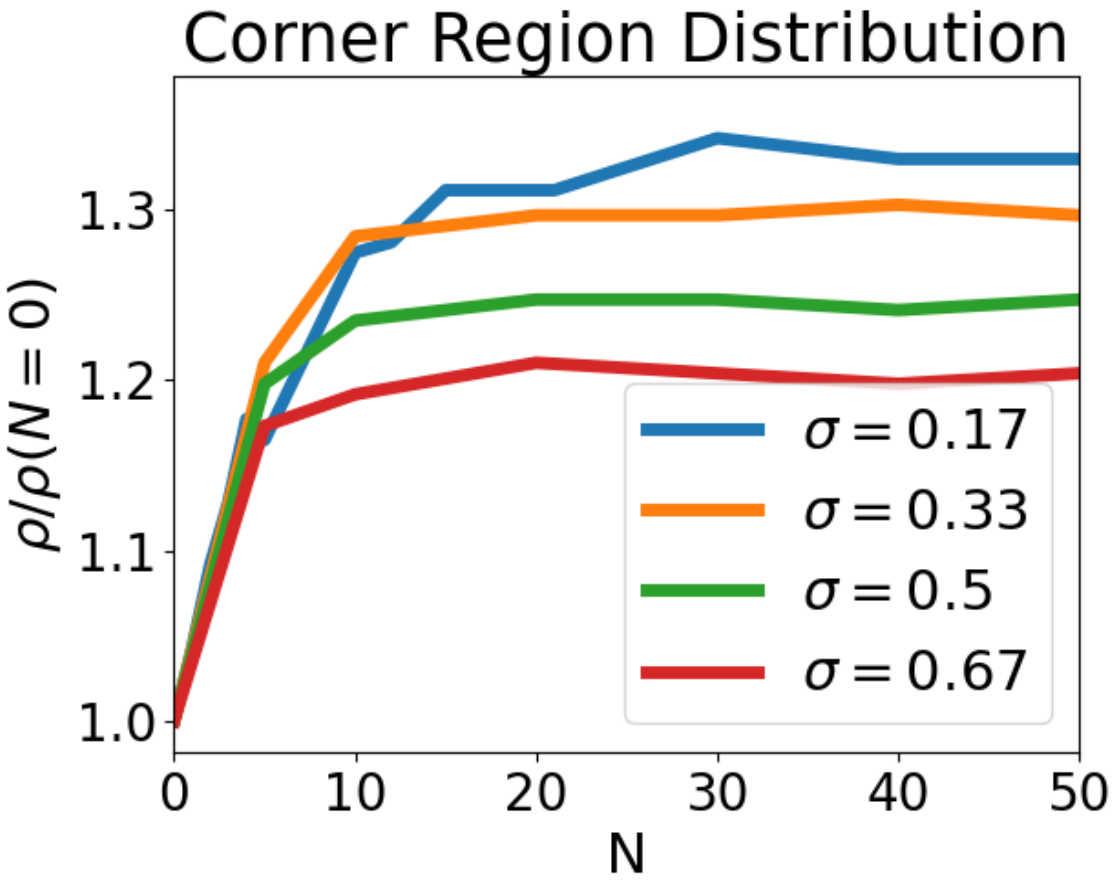

Figure 2.6: Relative change in ligand density on the corner region of the octahedron systems for different graft densities and ligand lengths.

    - increment h in the bin corresponding to $\vec{r}_{m_j}$

- Let the bin in h with the maximum number of counts be b_{max}
- Consider all bins in h with a number of counts greater than $\alpha \cdot b_{max}$ (with $.1 \leq \alpha \leq .25$) to be a point cloud with the point corresponding to each bin located at the center of the bin

After completing the algorithm described above and depicted visually on the top row of Fig. 2.7, we have a point cloud composed of points in our histogram h that have a sufficient number of counts. To get the vertices of the effective shapes, we determine the boundary of the point cloud, and then reduce the number of points on the point cloud while retaining its shape (Fig. 2.7, bottom).

The first of the two steps is finding the boundary of the point cloud. This was done through the matlab `boundary` function. The next steps are depicted visually in Fig. 2.7 and in the subsequent paragraphs.

The second of the two steps was done through the matlab `reducepatch` function. This function allows control over the number of faces on the shape, not the number of vertices, so many different numbers of faces were required to get the right number of vertices. Typically, the number of vertices we left in the final shapes was ≈ 100.

Once the vertices were determined, we needed to get the faces corresponding to the vertex set. This was done with the matlab `alphaShape` function, which takes one parameter, α. The value of α chosen was important because it controlled the concavity of the resulting shape: choosing an α value too large made the shape appear more convex than it is, whereas choosing an α value too small resulted in a shape with holes in it. In general, α values were chosen on a case-by-case basis and the α chosen was the minimum α such that there were no holes in the shape.

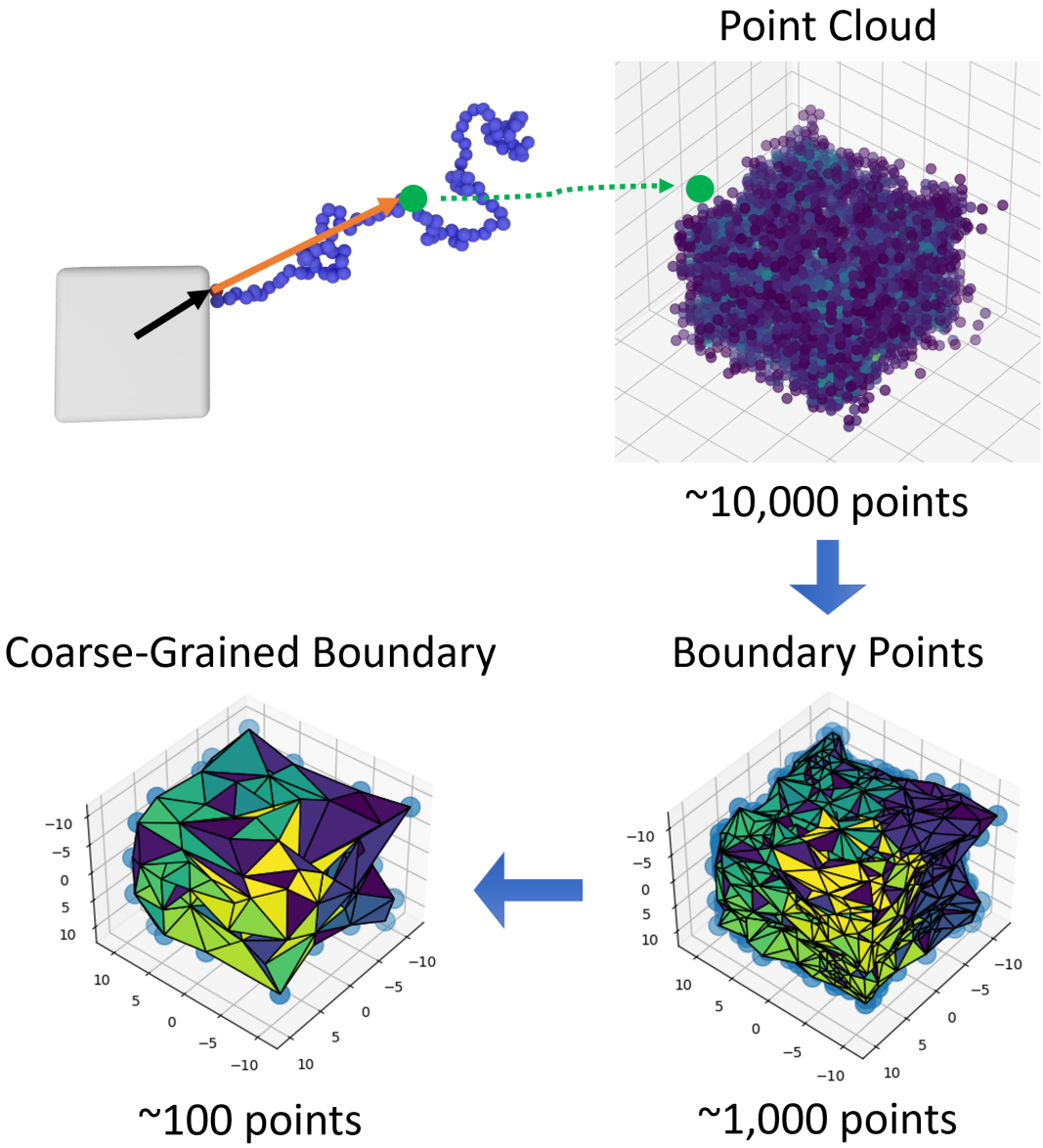

Figure 2.7: Visual depiction of the process by which we go from a simulation to an effective shape. The first monomer of the ligand chain to deviate significantly from a straight extension away from the core centroid is recorded and added to a histogram. The heavily populated histogram bins are translated back to positions which define the effective shape point cloud (top). The full algorithm is described in Section 2.5.3. Then, we identify the boundary of the point cloud, reduce the number of vertices, and define the faces of the resulting shape, which we define to be the effective shape (bottom).

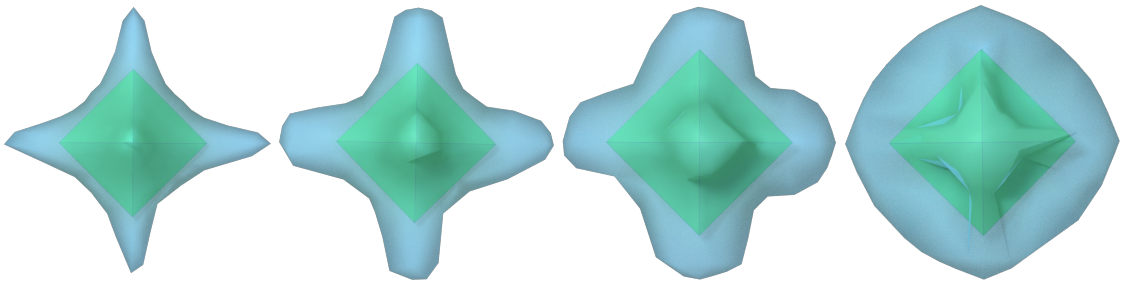

Figure 2.8: Transition from spiky phase to scooped phase for the octahedron with $N = 50$ and $f = 100, 200, 300, 400$ grafts. As f increases, the spikes gradually get thicker growing along the edges of the shape until they meet each other indicating the transition to the scooped phase. Depicted are the effective shapes as predicted by theory.

2.5.4 Gradual Transition from Spiky to Scooped Phases

The transition from spiky phase to scooped phase is a smooth transition. This gradual transition is best demonstrated in our octahedron systems. In Fig. 2.8, we show from theoretical calculations how the corner protrusions grow along the edges of the shape and eventually become scooped. One can see that as ligand density increases, the spikes become knobs, which get larger and larger until they merge with each ot?her along the edges of the shape, leaving only the faces of the shape unprotruded.

2.5.5 Theory Generalization for Elongated Shapes

Our theory assumes that all shapes are perturbations of spheres, i.e. the shape kernel Ω is defined as the distance to a point on the surface of the shape relative to the distance to the insphere for that shape along the same direction. For shapes that are elongated (i.e. $\Omega \geq 2.5$ somewhere on the surface), this perturbative assumption no longer holds. In such cases, we generalize the insphere to be an in-ellipse. The in-ellipse is defined as the largest ellipse that fits inside the core shape, similar to how the insphere is the largest sphere that fits inside the shape. We then alter the definition of Ω slightly as follows:

$$\Omega(\theta,\phi) = \frac{|\vec{r}_{core}(\theta,\phi)|}{|\vec{r}_{inellipse}(\theta,\phi)|}, \tag{2.4}$$

where $\vec{r}_{core}(\theta,\phi)$ is the vector to the point on the surface of the core at a direction defined by the angles θ and ϕ, and $\vec{r}_{inellipse}(\theta,\phi)$ is defined similarly. This generalization is ad-hock as it cannot be derived directly from the theory, so its predictions may not be accurate.

We apply the generalized theory to a pentagonal bipyramid system shown in Fig. 2.9. For this system, the ungeneralized definition of Ω can be as large as 3 at the bottom and top tips. We apply our generalized theory to the bipyramid, which predicts the effective shape diagram shown in Fig. 2.10. The simulation's rounded and spiky phases exist in the corresponding regions predicted by theory, however the theory predicts a transition to the scooped phase where one does not exist in simulation and there is no conformal region at lower graft densities like in the shapes that could be predicted with the ungeneralized theory. These results demonstrated our ad-hock generalization should not be heavily relied upon when working with elongated shapes.

2.5.6 Single Component Assembly of Scooped Cubes

As shown on the left in Fig. 2.11, the assembly of scooped cubes at filling fraction $\phi = 0.54$ results in a structure that has planes of simple cubic (left, yellow), but demonstrates a degree of orientational misalignment between the planes (right, red). By comparing this structure with the one obtained by adding the small spheres (right) at an equivalent filling fraction of cubes only ($\phi = 0.56$ scooped cubes + spheres), one can see the spheres remove the orientational misalignment between the planes of simple cubic. This demonstrates that not only is the scooped cube shape

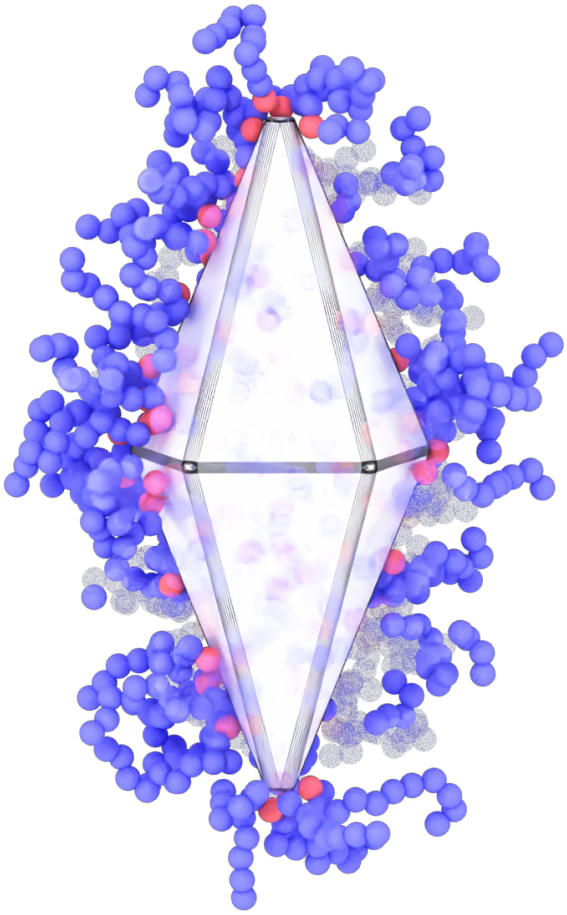

Figure 2.9: Elongated bipyramid.

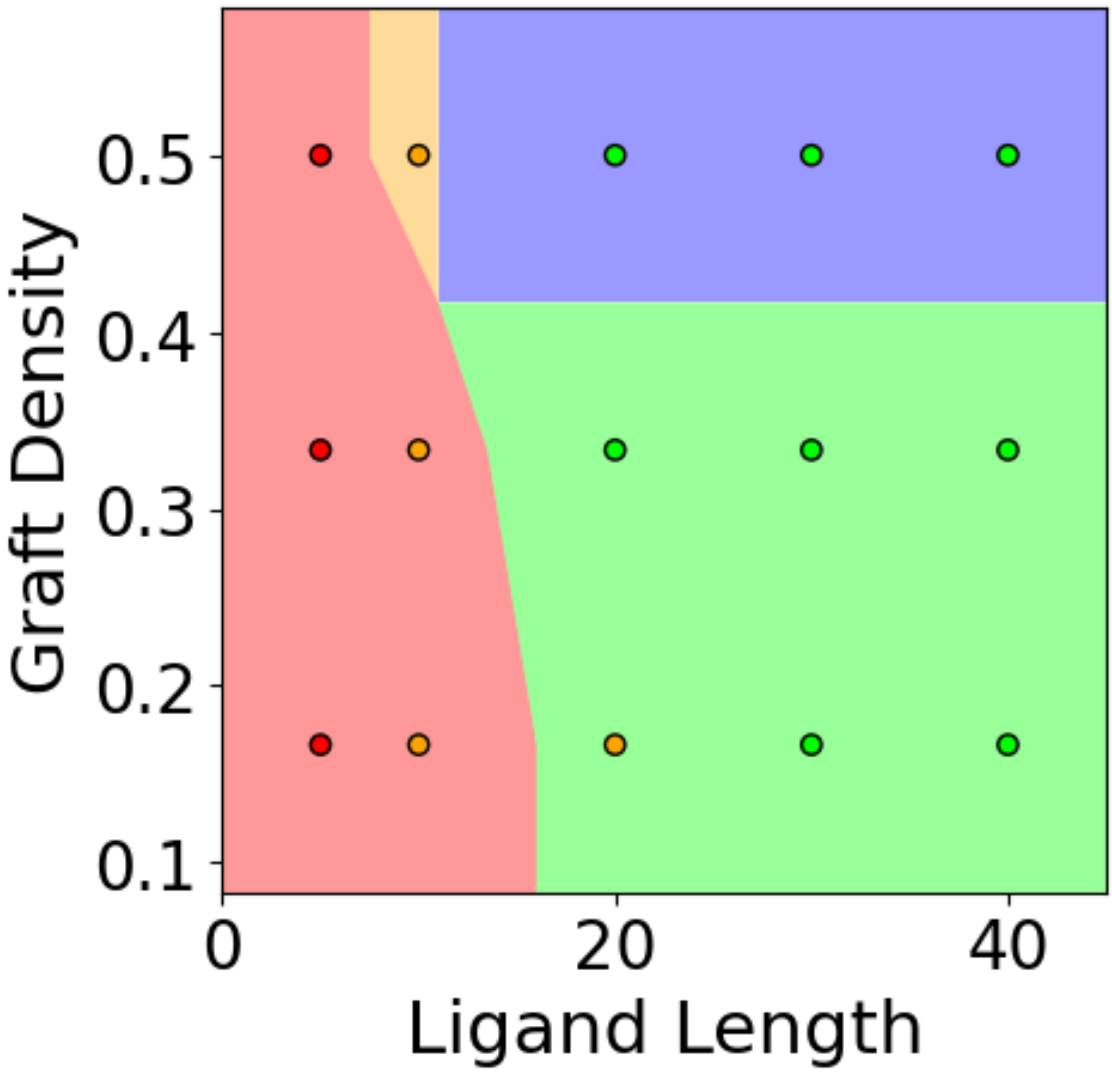

Figure 2.10: Effective shape diagram for the bipyramid systems. The diagram contains 4 effective shapes: rounded (red), conformal (orange), spiky (green), and scooped (blue). The background colors indicate the effective shapes predicted by theory, and the colored points indicate the effective shape observed in simulation.

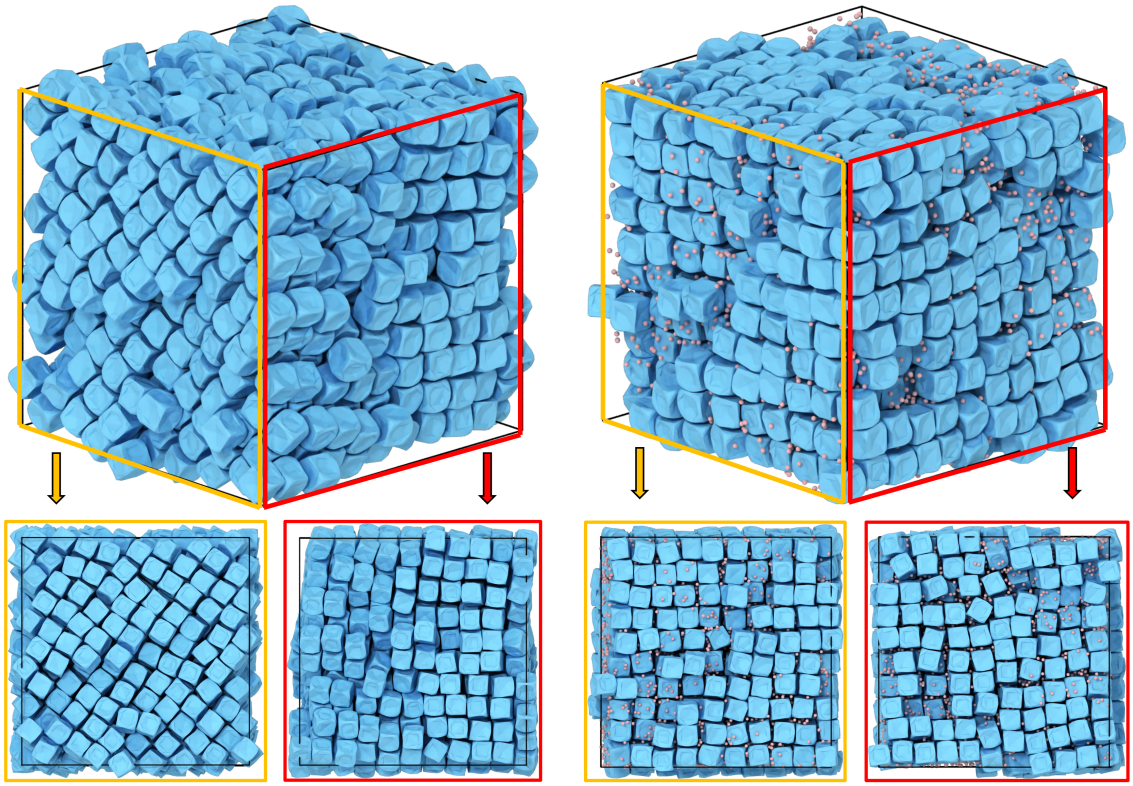

Figure 2.11: Comparison of single (left) and multi-component (right) assembly of scooped cubes at filling fractions of $\phi = 0.54$ and $\phi = 0.56$, respectively. We find that scooped cubes assemble into planes of simple cubic (yellow) exhibiting stacking misalignment along the third dimension (red). In the multi-component case, we see simple cubic formation along all three dimensions, demonstrating that spheres act as depletants stabilizing the orientational misalignment between layers of simple cubic.

able to localize the smaller spheres, the structure formed by the scooped cubes is further stabilized by the sphere's presence.

CHAPTER III

"Atomic Stencil" for Precise Polymer Patch Formation on Gold Nanoparticles

The work in this chapter is part of a collaboration with the Chen group at the University of Illinois at Urbana-Champaign, the Fichthorn group at Penn State, and Thi Vo at The Johns Hopkins University. Our collaborators in the Chen group performed all the experimental work, the Fichthorn group performed all the DFT calculations, and Thi performed all the theory calculations. The contents of the this chapter are reproduced (with some modification) from a joint manuscript now being prepared for publication in a journal.

3.1 Introduction

Patterning nanoparticles (NPs) with patches with predictive control over patch size, shape, placement, and number is a holy grail of NP assembly research, potentially applicable in nanorobots[89], targeted delivery[90], and assembly into optical and mechanical metamaterials[91, 92]. However, patterning at nanometer scales remains challenging to create large-scale, uniform particles with intricate patch patterns. This often leads to low-quality and inhomogeneous patches on the NPs, resulting in low yields and a lack of large-scale assembly. To provide a versatile and definitive method to control patch patterning, the Chen group designed a new plat-

form enabling precise nanoscale patch-patterning, inspired by "stencil" methods. In their design, the iodine adatom "mask" gold NP surfaces to induce selective polymer grafting to be "painted" on NP surfaces with controlled patterns and sizes.

We demonstrate the atomic stencil method on a library of differently shaped NPs, resulting in unprecedented precision and homogeneity in various molecular patterning. There, the iodine adatom is first utilized as a "mask" to induce selective polymer grafting on gold NP surfaces. Then the patch patterning is achieved through short ligand absorption on less-effectively "masked" regions and subsequent physisorption of polymer molecules. The Chen group experimentally show that this method can be universally applicable to create a library of patchy NPs, including gold octahedra, cubes, rhombic dodecahedra, cuboctahedra, and bipyramids. We lay out the foundation for this new design principle by using DFT calculation of adatom interactions with different facets of gold surfaces. Thiol-gold bonding is formed on the remaining surfaces to enable facet-specific spatial organic molecular patterning. The versatility of the strategy is explored with a combination of experiments, polymer physics scaling theory, and molecular simulation. Our method is applied to NPs with different shapes to generate a range of patterns, from having patches on the vertices to the faces, in agreement with theory and MD simulation. For example, by utilizing both octahedron and rhombic dodecahedron, we can manipulate patch size on NP surfaces without changing their spatial location (vertex and face, respectively), by altering iodine incubation concentration.

The resulting polymer-patched gold NPs are highly uniform, stable, and well-dispersed in water. As a proof of concept, we demonstrate large-scale patchy NP assemblies, resulting in highly ordered open lattices. Our open lattices assembled from patchy octahedra, cubes, cuboctahedra, and rhombic dodecahedra display di-

rectional, large interparticle spacing, which is not achievable with conventional NPs with homogeneous surface chemistry and topography. X-ray tomography revealed that patchy rhombic dodecahedrons form body-centered cubic (BCC) lattices, different from the closely packed lattices that bare rhombic dodecahedron gold NPs form. Hard Particle Monte Carlo (HPMC) simulations further reveal that site-specific and directional interaction among precisely patterned patches on NPs creates these open-lattice structures. We anticipate that our strategy will aid the rational design and fabrication of organic molecular patterns on the NPs for their use in targeted delivery, sensing, nanorobots, and their assembly into open lattices for applications in shock-absorption, heat dissipation, and lattice plasmonics.

3.2 Adatom-Directed Polymer Patch Stencil on Gold Nanoparticles

We draw inspiration from the stencil method, a two-step process that enables easy patterns with exact details on the surface of 3D objects. First, a mask is applied to the surface, and then paint is applied over the mask to create the pattern (Fig. 3.1a). We propose using a stencil approach at the nanoscale, using adatoms and thiol molecules as a "mask" and "paint". This combination meets three key requirements for atomic stencil. First, the mask must have selective absorption at specific sites. Second, the mask should be robust enough to withstand the painting process without being removed. Third, the mask should be resistant to any paint covering the surface. To achieve such, we utilize the trace amount of iodine adatom in combination with thiol ligands on the faceted gold NPs. We propose a thermodynamically mediated strategy for molecular patterning on high-curvature NPs involving the absorption of iodine adatoms onto gold surfaces and thiol ligands onto the remnants of the masked area (Fig. 3.1b).

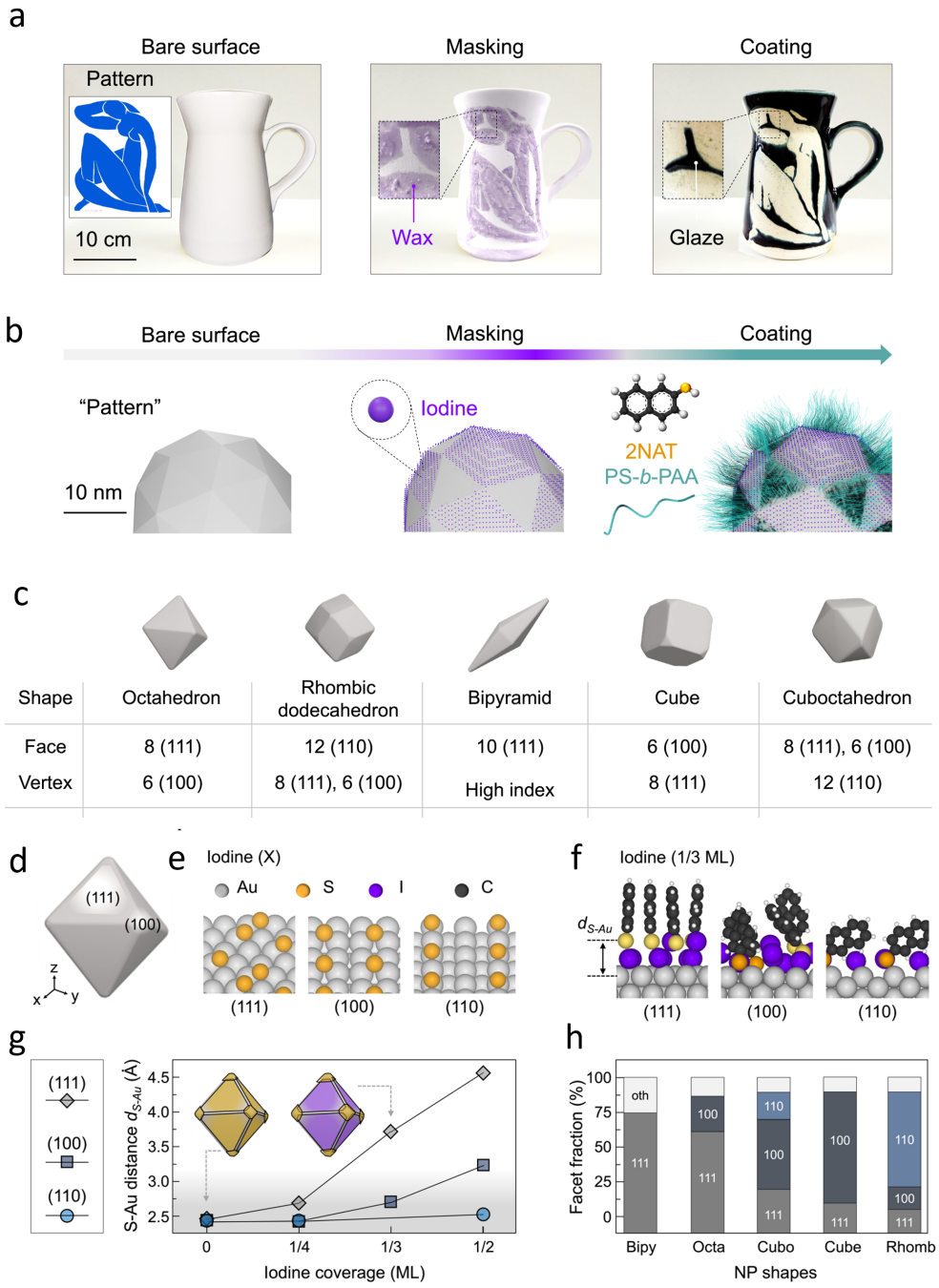

Figure 3.1: Strategy for the synthesis of iodine masked patchy NPs, as proposed by the Chen group. (a and b) We give an analogy for the "stencil" method: A mask is placed on the surface of an object and afterwards the desired coating pattern is achieved due to the properties of the mask. (c) We demonstrate our library of shapes and detail the shape faceting, which drives the iodine attachment process. (d) We show visually the faceting on the octahedron. (e, f, g, h) The DFT calculations of the S-Au distance on different NP facets.

Such adatom absorption has also been utilized during the NP growth to guide faceted NPs and overgrowth of inorganic NPs[93, 94, 95] but has not been used for precise molecular patterning at the organic/inorganic interfaces. Although bromine and chlorine can also be absorbed onto gold surfaces in a facet-dependent manner, their absorption is primarily physical rather than chemical, and thus can be easily removed. In contrast, we will show iodine chemisorbs onto the gold surface to form a strong Au-I bond, providing a stable "mask" for thiol ligands to absorb onto the remaining area not covered by iodine. The thiol-coated area allows amphiphilic polymers to physisorb and form polymer patches.

DFT calculations by the Fichthorn group on bare gold surfaces shows that on low index gold facets, 2-naphthalene thiol (2-NAT) ligands can absorb to form stable, chemical Au-S bonds on all three facets, as characterized by short S-Au distance below 2.5Å (Fig. 3.1e,g). However, when iodine is present, thiol ligands exhibit different absorption on gold surfaces for different facets, resulting in site-selectivity in absorption. In the presence of iodine at a surface coverage of 1/3, Au (100) and (110) surfaces chemisorb in between the adatoms to make stable S-Au distances of < 3Å (Fig. 3.1g). On the Au (111) surface, the distance between S and Au increases to 3.7Å, indicating the instability of thiol absorption, presumably due to the sulfur not being chemisorbed onto the gold surface underneath the highly-packed iodine adatoms. The face-centered crystalline structure of gold determines the different corresponding surface-enclosing facets of these particles. In Fig. 3.1c, we show the faceting on each face of our shape library.

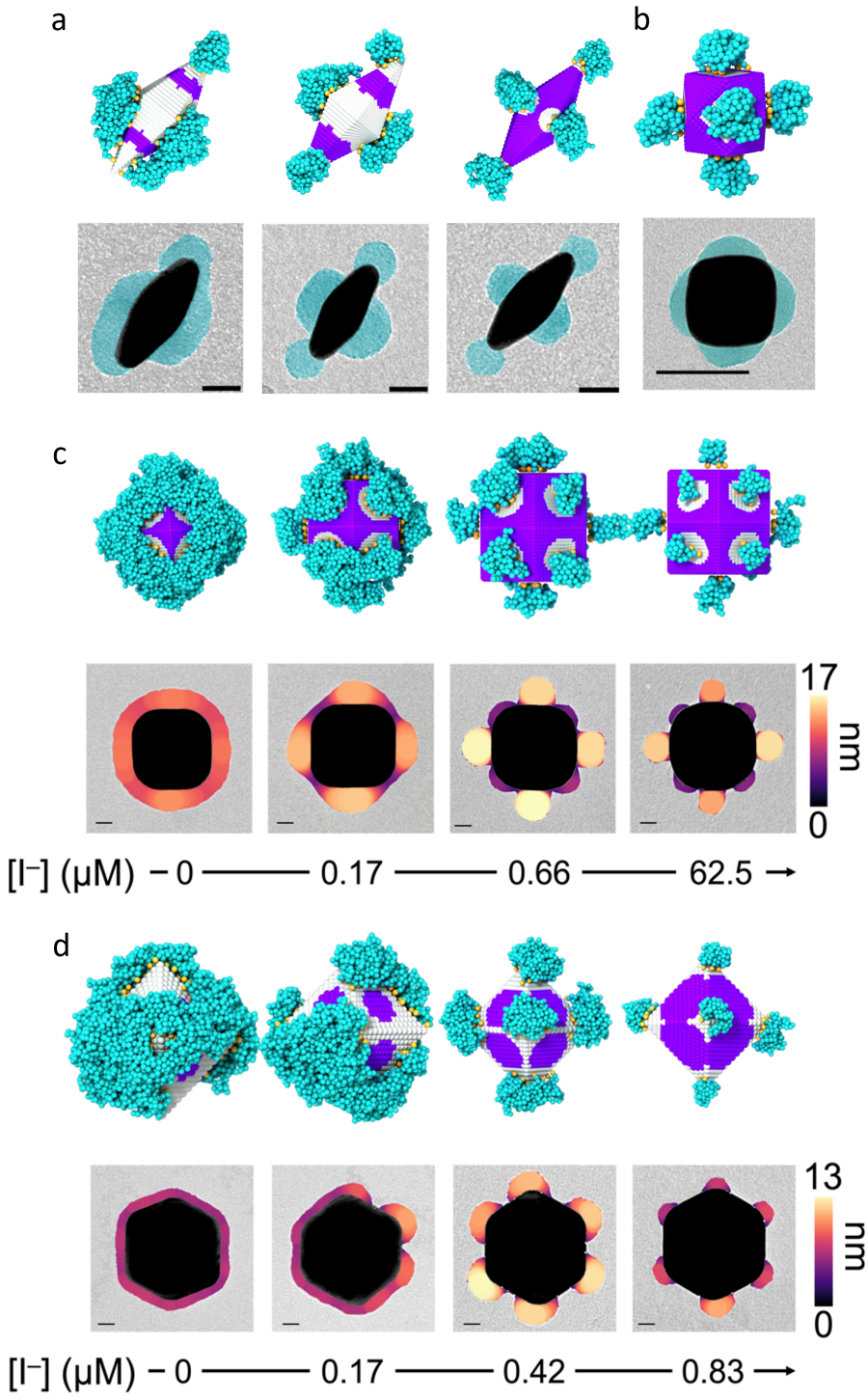

Figure 3.2: Experimental and simulated NP shapes and patch patterns. (a) Three patterns for the bipyramids. (b) Face patched pattern for cuboctahedra. (c) Transition in rhombic dodecahedra when increasing iodine concentration. (d) Transition in octahedra when increasing iodine concentration. On the simulated NPs, the sea of purple points are the "iodine" regions and the sea of white points are the "2-NAT" regions. Experimental images provided by the Chen group.

3.3 Patchy Gold Nanoparticle Synthesis

The Chen group experimentally demonstrated the effectiveness of the atomic stencil approach. They synthesized gold NPs with different shapes including octahedron, rhombic dodecahedron, cuboctahedron, and bipyramid. The surfaces of the particles were initially stabilized with cetyltrimethylammonium bromide (CTAB). During the atomic stencil process, the NPs are submerged in an iodide solution, which replaces the bromine-based surfactant on the surface of the NPs with iodine. Noteworthily, the incubation has been carefully controlled as excess iodine can cause oxidative etching of gold NPs and reduce Au NPs surface stability. After washing the particles to remove the remaining iodine, they are incubated in an aqueous solution (DMF to water ratio of 4.5:1) with 2NAT, short hydrophobic thiol ligands, and polystyrene-b-polyacrylic acid (PS-b-PAA, 20,000 g/mol). During the incubation, the polymers physisorbed onto the hydrophobic ligand-coated area on gold NPs by hydrophobic attraction, resulting in site-specific decorated patches. In Fig. 3.2, we show patch patternings on our stenciled NPs for each shape studied. The presence of face-patched NPs for many of the shapes demonstrates the use of iodine as an experimental design handle to control patch location, as particles with no iodine applied would either exhibit no patches or a corner-patched pattern[96].

To further understand the physical mechanism behind the patch pattern formation, we model the system interactions and use MD simulations to get a detailed view of the polymer behavior. To simulate the masked NPs, we begin by using a theoretical model based on DFT calculations performed by the Fichthorn group and the experimental iodine concentration to determine which regions of the NP surface are covered with iodine. We then place a sea of "iodine" particles on the surface

of those regions and a sea of "2-NAT" particles in the other regions to model the interactions the polymers experience while physisorbing onto the NP core surface. Once the core surface is covered with particles to model the correct interactions, we place polymer chains on the NP and run the simulation, allowing the polymer chains to equilibrate and form patch patterns. For full simulation protocol details, see Section. 3.5.1.

We show our simulated stenciled particles in Fig. 3.2. The bipyramids (a), cuboctahedra (b), rhombic dodecahedra (c), and octahedra (d) all demonstrate good agreement between patch patterns in experiment and simulation. The patch pattern trend highlighted in Fig. 3.2a,c,d demonstrates that increasing iodine concentration restricts more of the core surface area, fracturing a single NP-spanning patch into many smaller patches, whose location is determined by the iodine mask. This trend demonstrates the utility of iodine concentration as an experimental design handle for NP patch size and count.

3.4 Large Scale Assembly into Open Lattices

With the interactions and patch behavior at the level of a single NP now understood and, with demonstrated agreement between simulation and experiment, we next turn to understanding the large-scale assembly of stenciled NPs. We assemble four different stenciled NPs: face-patched rhombic dodecahedra, face-patched cuboctahedra, corner-patched octahedra, and face-patched truncated cubes. Experimental assemblies of each shape are shown in Fig. 3.3, with each structure assembling into either a BCC or BCT lattice in the case of the truncated cube (Fig. 3.3e).

To simulate these assemblies, we first build a simulation model that accounts for the interactions introduced by the iodine stenciling and patch formation on the NPs.

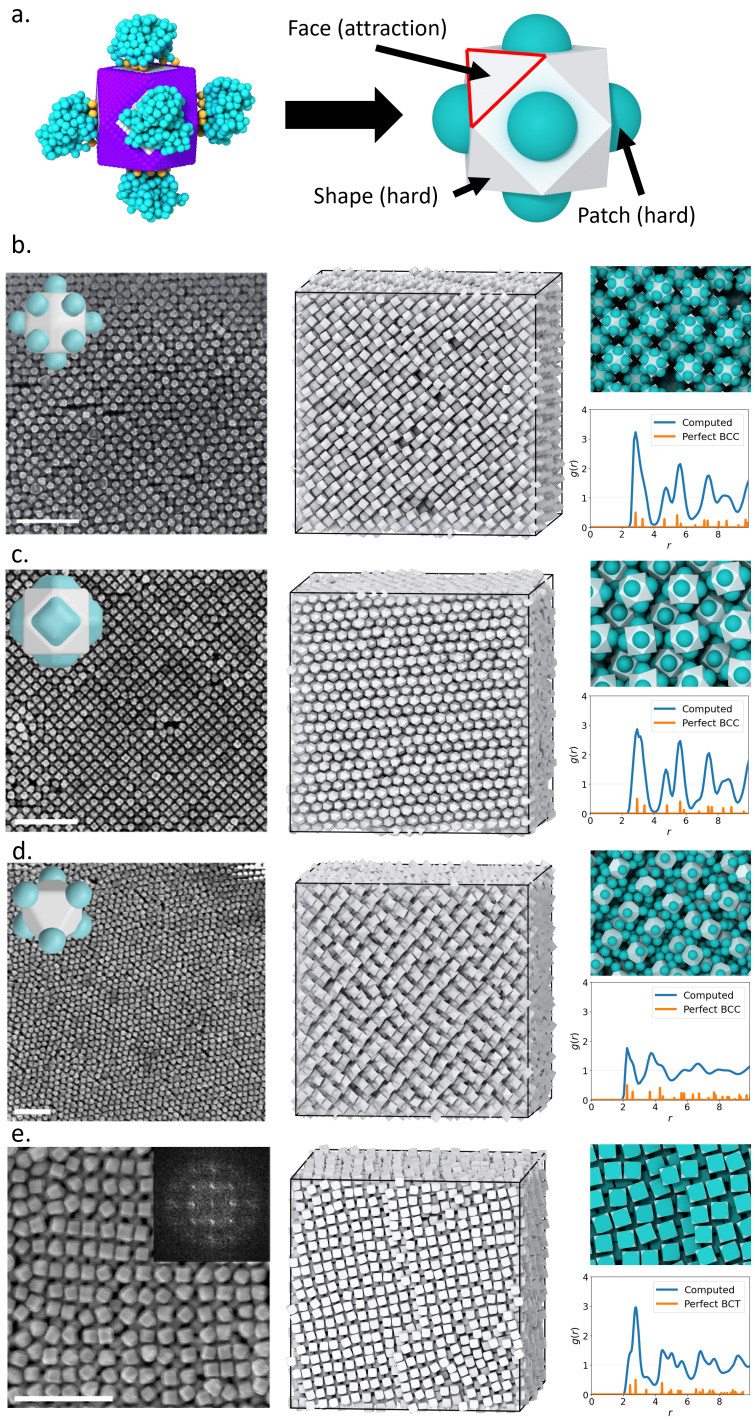

Figure 3.3: Simulated assembly of patchy particles into self-assembled crystals. (a) We abstract the patch patterns from the single NP simulations in the previous section to simulate their large-scale assembly in HPMC. We use a directional, short-range interaction on each face which is not covered by a patch to drive the assembly behavior. (b, c, d, e) We compare the Chen group's experimentally assembled structures (left column) to the structures assembled in simulation (center column, rendered without patches). (right column) We show a close-up view of the assembled structures and the system RDF, demonstrating their assembly into BCC and BCT structures. Experimenal images provided by the Chen group.

The patches are formed by the PS-b-PAA polymer chains, whose outer layer is PAA. Two interacting patches on adjacent NPs therefore exhibit steric repulsion between PAA molecules, so we model the patches as "hard" in simulation. Iodine-covering of shape facets prevent patch formation in those locations, leaving the Au atoms of the NP core available to interact with Au atoms on adjacent NPs via van der Waals forces. We therefore model a short-range, directional attraction between exposed (111) NP facets. A summary of our simulation model is depicted in Fig. 3.3a.

We then run HPMC simulations detailed in Section 3.5.2 for the assembly of these particles. Our assembly results are shown in the center and right columns of Fig. 3.3. The rhombic dodecahedra, cuboctahedra, and octahedra assemble into BCC structures at the low filling fractions of $\phi = 0.45$, $\phi = 0.47$, and $\phi = 0.37$, respectively. The truncated cubes assemble a BCC-like structure at the filling fraction of $\phi = 0.33$ and transition to a BCT lattice at the filling fraction of $\phi = 0.53$ (BCT shown in Fig. 3.3e). All simulation results are consistent with experimental results in the left column of Fig. 3.3.

To understand the observed assembly behavior, we first notice that 3 of the 4 shapes: truncated cubes, cuboctahedra, and octahedra are in the same shape family: cubes with varying degrees of tip truncation. Tip truncation in this shape family exposes the (111) plane of the NP Au core, causing the iodine to attach, preventing patch formation, and inducing inter-NP attraction. Furthermore, attractive forces on the 8 truncation planes create the local bonding environment of a BCC lattice and induce assembly into a BCC crystal. The truncated cubes assembly into a BCT structure with lattice vector ratios $1.8 : 1 : 1$ because a BCC crystal of that shape cannot exist at a filling fraction $\phi = 0.53$, so the structure is altered along one dimension. The case of the rhombic dodecahedra is similar to the previous three

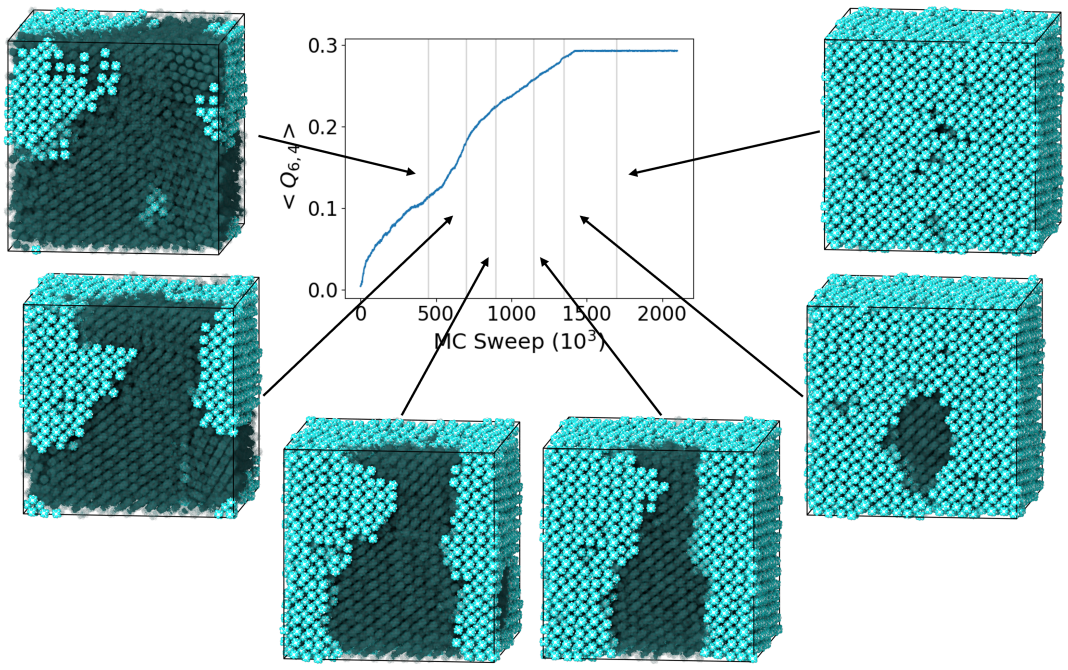

Figure 3.4: A visual depiction of the assembly pathway in the assembly of the patch rhombic dodecahedron system. We plot the system-averaged Steinhardt $Q_{l=6,m=4}$ harmonic vs. simulation step. The system undergoes a steady transition from many grains of differently oriented BCC (transparent) into a single BCC crystal grain.

shapes, except that the corners are covered with iodine rather than faces, creating opportunities for bonding along the directions associated with its vertices. 8 of the rhombic dodecahedron's 14 vertices share the same local environment of the BCC's first neighbor shell, just like the previous shapes. Additionally, the 6 other vertices have the local orientation of the BCC's second neighbor shell. To summarize, the iodine locations determine the NP attractions and local bonding environment, which then drive the system's crystallization behavior. These patchy particle assemblies are therefore unique in that the assembly behavior is driven not by where the patches *are*, but where the patches *aren't*.

3.4.1 Assembly Pathway

In addition to the equilibrium crystal structures assembled by the patchy NPs, in simulation we study the assembly pathway for each of our shapes. Qualitatively, each shape behaves similarly: many grains of the final crystal at different orientations form very quickly. Further merging of the different grains is kinetically slow in the experiments, preventing the formation of a single grain. We anneal the systems by running our simulations at higher temperatures, allowing the system to relax and allowing neighboring misaligned grains to merge into a single final crystal. We then slowly cool the system back down to the original temperature. Fig. 3.4 demonstrates the process of neighboring misaligned grains slowly ripening into a single crystal grain for the rhombic dodecahedron system. We use the steinhardt $Q_{6,4}$ harmonic as a local order parameter[97] to pick out particles that have the orientation of the final crystal grain.

3.5 Methods

3.5.1 Polymer Patched Particle Simulations

We run molecular dynamics simulations in HOOMD-blue[79] of octahedron, cuboctahedron, rhombic dodecahedron, and bipyramid NPs grafted with polymer bead chains of length $N = 16$ and diameter $b = 0.7$ at nominal graft densities ranging from $\sigma = 0.083$ to $\sigma = 0.45$. The parameters N and b are chosen consistent with the parameters of the experimental polymer, and σ is chosen consistent with experimental NP surface coverages.

For simulating particles with shape in molecular dynamics, we use the anisotropic Lennard-Jones (ALJ) pairwise interaction potential[83], as used in Chapter II. We chose ALJ interaction strength parameters the same as used in Chapter II, with the

only difference being $\epsilon_{monomer-monomer} = 3$ to model the hydrophobic interactions of the PAA blocks on the polymer. We chose ALJ diameters for the core particles to be their insphere diameter, and 1 for the graft and monomer beads.

We model the polymer chains with an attractive bead-spring model, where each monomer is bound to its adjacent monomers by a combined FENE + WCA potential

$$U_{FENE+WCA} = -\frac{1}{2}kr_0^2 ln\left[1-\left(\frac{r}{r_0}\right)^2\right] + 4\epsilon\left[\left(\frac{\sigma}{r}\right)^{12} - \left(\frac{\sigma}{r}\right)^6\right], \tag{3.1}$$

where $k = 70$, $r_0 = 1.725$, and ϵ and σ are chosen consistent with their values for the ALJ pairwise potential. These parameters were chosen consistent with Chapter II, which demonstrated good solvent scaling for polymer chains without attractions.

We simulate surface masking by adding a dense coating of repulsive "poison" particles to core surface regions predicted to be covered by iodine by DFT and theory calculations. The poison particles only interact with the graft particles and have solely repulsive interactions with parameters $\epsilon = 5$ and $\sigma = 1.05$. We generate these coatings via the *agrippa*[82] package, discussed in Chapter V of this thesis.

We run simulations in the NVT ensemble with $kT = 1.0$ and a simulation timestep of $dt = 0.0001$. We first run simulations for 10^7 timesteps without monomer-monomer attractions so the chains could both migrate to the non-poisoned regions of the core and reach an equilibrated chain conformation. After this period, the attractions between the monomers were set to the values from the previous paragraphs and the simulations were run for another 10^7 steps.

3.5.2 Nanoparticle Assembly Simulations

We model the PAA-PAA steric repulsion between the nanoparticle polymer heads with hard sphere interactions at patch locations on the core surface. We chose a hard sphere radius, which maintains relative patch size (R_{patch}/R_{core}) between

simulation and experiment. We model the Au-Au van der Waals attractions between nanoparticle cores with a directional, short-range interaction potential at each face that contains no patch. For the rhombic dodecahedra, we place the potential at each corner containing no patch. The interaction potential between two points $\vec{r}_i$, $\vec{r}_j$ on particles with orientation Ω_i, Ω_j is defined by:

$$U(\vec{r}_i, \vec{r}_j, \Omega_i, \Omega_j) = \begin{cases} 0 & \text{if } r_{ij} > \sigma \\ -\epsilon f(\Omega_i, \Omega_j) & \text{if } r_{ij} <= \sigma \end{cases} \tag{3.2}$$

where $\epsilon > 0$ is the attraction strength, σ is the attraction distance, and

$$f(\Omega_i, \Omega_j) = \begin{cases} 1 & \hat{e}_i \cdot \hat{r}_{ij} > cos(\delta/2) \text{ and } \hat{e}_j \cdot \hat{r}_{ji} > cos(\delta/2) \\ 0 & \text{otherwise} \end{cases} \tag{3.3}$$

where $\hat{e}_\alpha$ is the director of the interaction on particle α and δ is the interaction opening angle. We use parameters $\epsilon = 3.0$, $\sigma = R_{core}$, and $\delta = \pi/4$.

We ran Monte Carlo simulations of $N = 10,000$ particles with the HOOMD-Blue simulation toolkit using the simulation model described above for face-patched rhombic dodecahedra (filling fraction $\phi = 0.45$), face-patched cuboctahedra ($\phi = 0.47$), corner-patched octahedra ($\phi = 0.37$), and face-patched cubes ($\phi = 0.53$ and $\phi = 0.33$). To get final assemblies consisting of a single crystal grain, simulations were annealed from initial temperature $kT = 1.0$ up to a final temperature between $kT = 1.2$ and $kT = 2.0$, and slowly cooled back down at the end. We ran the annealing step for 4×10^6 MC sweeps and cooled the simulation slowly for 3×10^6 MC sweeps.

3.6 Conclusions

We have demonstrated the utility of a new stencil method for control of patch size and location on the surface of anisotropic NPs. By using iodine and 2-NAT

adatoms, we are able to leverage the faceting of the FCC gold lattice from which NPs are synthesized to alter the attachment energy of the adatoms, and therefore patches, to different locations on the NP surface. DFT calculations were carried out by the Fichthorn group and a theoretical model developed was by Thi Vo to compute the relative polymer attachment energy to each facet of the NP surface as a function of the iodine concentration. We used the attachment energy information to create a simulation model validating the physical assumptions about the interactions driving the patch patterns found in experiment. We then simulated four NP shapes at a variety of iodine concentrations and graft densities demonstrating agreement between simulation and experiment. The transitions between patch patterns demonstrate iodine concentration as an experimental handle to control the patch size and location. We then abstract our simulation model for the individual NPs, simulating their large-scale assembly into BCC and BCT lattices, consistent with the experimentally assembled structures. Furthermore, we understand the assembly of the patchy NPs to be driven by the exposed (111) iodine-covered facets rather than the patch-covered locations of the NP surface.

3.7 Supplementary Information

3.7.1 BCC to BCT Transition in Truncated Cubes

All shapes in this project form BCC-like structures at intermediate volume fractions, with the truncated cube being the only shape to form a BCT rather than a BCC. In Fig. 3.5a, we show that the truncated cube forms the BCC structure at a lower volume fraction, where the shape and bonding geometry do not prevent BCC formation like at intermediate volume fractions (Fig. 3.5b). Due to thermal fluctuation and the large amount of open space in the lattice, the first two peaks of the perfect BCC crystal appear as a single large peak in the computed pair correlation

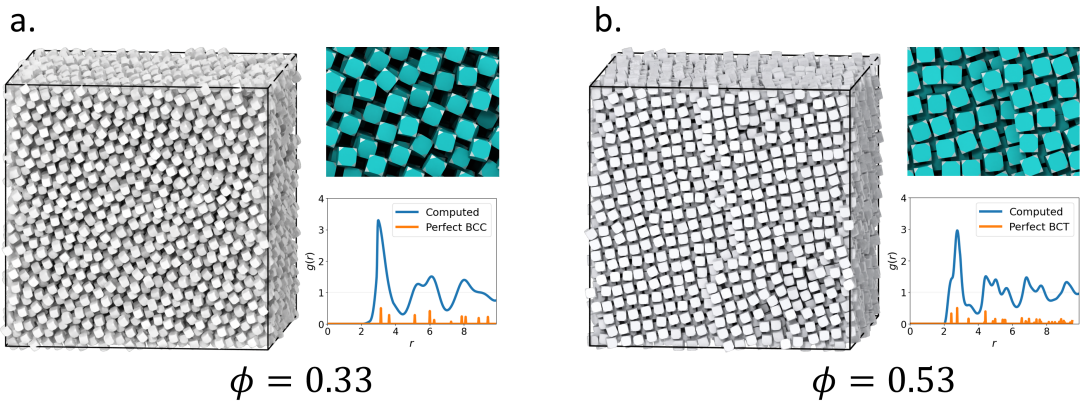

Figure 3.5: BCC to BCT transition in truncated cubes. (a) The BCC structure formed by the truncated cubes at volume fraction $\phi = 0.33$. At a higher packing density this structure cannot exist and the lattice shears along one dimension to create a BCT. (b) The BCT structure formed by the truncated cubes at volume fraction $\phi = 0.53$. The lattice vector length ratio in the BCT is $1.8 : 1 : 1$.

function $g(r)$. At $\phi = 0.53$, the system retains its body-centered geometry, but the unit cell is sheared along one dimension to fill the box at $\phi = 0.53$. The lattice vectors of the resultant BCT structure have ratios of $1.8 : 1 : 1$.